symmetry

MDPI

Article

Orientation-Dependent High-Order Harmonic Generation from Monolayer ZnO

Zijian Hu [1,2], Xiance Xie [1,2], Zhihong Yang [1], Yunhui Wang [1,*] and Shicheng Jiang [2,*]

[1] New Energy Technology Engineering Laboratory of Jiangsu Province, Information Physics Research Center, School of Science, Nanjing University of Posts and Telecommunications, Nanjing 210023, China
[2] State Key Laboratory of Precision Spectroscopy, East China Normal University, Shanghai 200062, China
* Correspondence: yhwang@njupt.edu.cn (Y.W.); scjiang@lps.ecnu.edu.cn (S.J.)

Abstract: Solid-state high-order harmonic generation (HHG) now is a strong tool for detecting target properties, like band structure, Berry curvature and transition dipole moments (TDMs). However, the physical mechanism of high-order harmonic generation (HHG) in solids has not been fully elucidated. According to previously published works, in addition to the inter-band polarization, intra-band currents, and anomalous currents due to Berry curvature, there is another term which will be called the mixture term (MT). Taking monolayer ZnO as a sample, it is found that the intensity of the mixture term, which has been ignored for a long time in previous works, actually is comparable with other terms. Additionally, we compare the orientation-dependent HHG spectra that originated from different mechanisms. It is found that the inter-band and mixture HHG show similar orientation features. Meanwhile, Berry curvature only produces perpendicularly polarized even harmonics, and intra-band perpendicularly polarized even harmonics show special orientation features which can be explained by the orientation-dependent group velocity. This work will help people understand the mechanisms of solid-HHG better.

Keywords: high harmonic generation; Berry curvature; laser-induced current

Citation: Hu, Z.; Xie, X.; Yang, Z.; Wang, Y.; Jiang, S. Orientation-Dependent High-Order Harmonic Generation from Monolayer ZnO. *Symmetry* **2023**, *15*, 1427. https://doi.org/10.3390/sym15071427

Academic Editors: Palle E.T. Jorgensen and Hung T. Diep

Received: 31 May 2023
Revised: 4 July 2023
Accepted: 12 July 2023
Published: 15 July 2023

1. Introduction

High-order harmonic generation (HHG) is a nonlinear optical process, and under the irradiation of a strong laser, the coherent radiation emitted by the macroscopic system is many times the frequency of the driving laser field. In past decades, people have studied the high-order harmonics generated by strong laser pulses in gas, which provide new extreme ultraviolet and soft X-ray light sources. HHG in gas promotes the generation of an attosecond pulse, which in turn promotes the detection and control of electrons to an attosecond time scale, and lays a foundation for attosecond science [1,2]. Due to the high density and periodic structure of crystals, solid materials can achieve more intense harmonic signal than atoms and molecules. Since Ghimire et al. [3] observed nonperturbative HHG from ZnO in 2011, HHG has been observed in semiconductors [4–7], rare gas solids [8], monolayer materials [9–12], doping systems [13,14] and topological insulators [15,16]. Solid-state HHG has great promise as a novel attosecond light source, as well as novel ultrafast spectroscopy methods probing topological effects [15,16], band structure [17,18], Berry curvature [10,19] and transition dipole moments [20–22].

For the mechanisms of HHG from gaseous medium, Corkum and kulander [23,24] described it with a semiclassical three-step model in 1993. After Ghimire et al. Observed HHG in bulk crystals, several experimental [5,7,25] and theoretical studies [26,27] had been carried out to understand its detailed microscopic mechanisms of solid-state HHG. The recollision model for gas-phase HHG was then extended to the condensed phase, e.g., ionization acceleration and recombination [26,27]. This picture has been clarified by time-dependent strong-field light-matter simulations, such as time-dependent density

functional theory (TDDFT) [28,29], a time-dependent Schrödinger equation (TDSE) [13,27] and semiconductor Bloch equations (SBEs) [30–32]. According to the three-step model, the laser-induced current includes intra-band current and partial derivative of inter-band polarization with respect to time. Additionally, it should also contain the Berry curvature induced anomalous current induced by Berry curvature [19,33] which was frequently discussed previously in the adiabatic regime. Actually, as early as 1995, C. Aversa and J. E. Sipe showed that there is another mixture term that would produce current inside the crystal [33]. For a long time, this term was ignored in the research on solid-state HHG. Later, J. Wilhelm et al. [34–36] recall the mixture term which can also be on the HHG spectrum. To date, research on the mixture term induced HHG is still lacking.

In this paper, we will explore the orientation-dependent feature of HHG spectra generated from different mechanisms by solving the SBEs numerically. It is found that the orientation-dependent feature of mixture term-induced HHG is similar to that of inter-band polarization-induced ones. However, the intra-band perpendicularly polarized component shows a very different orientation-dependent feature, which can be explained by the orientation-dependent group velocity. Our results stress again that in some specific orientation angles and high harmonic orders, the mixture term-induced spectrum is comparable or even higher than intra-band components. The mixture term-induced HHG is a component that cannot be neglected in future research.

2. Sample and Equations of Motion

In this work, we will take monolayer ZnO as a sample. Monolayer ZnO is a graphene-like two-dimensional honeycomb lattice. Graphene-like monolayer was first predicted via theoretical simulation [37,38] and then produced in the experiment [39]. In this work, we use the tight-binding model including s orbital of Zn atom and p_x, p_y orbitals of the O atom, to model the monolayer ZnO. The constructed Hamiltonian reads

$$\mathrm{H}(\mathrm{k}) = \begin{bmatrix} \varepsilon_{Zn}^{s} & g_1 h_{sp} & \frac{\sqrt{3} g_2 h_{sp}}{2} \\ g_1^* h_{sp}^* & \varepsilon_O^{p_x} & 0 \\ \frac{\sqrt{3} g_2^* h_{sp}^*}{2} & 0 & \varepsilon_O^{p_y} \end{bmatrix} \tag{1}$$

with

$$g_1(\mathbf{k}) = -e^{ik_x L/\sqrt{3}} + e^{-ik_x L/2/\sqrt{3}} \cos(k_y L/2), \tag{2}$$

$$g_2(\mathbf{k}) = -e^{-ik_x L/2/\sqrt{3} + iLk_y/2} + e^{-iLk_x/2/\sqrt{3} - iLk_y/2}. \tag{3}$$

ε_{Zn}^{s} and $\varepsilon_O^{p_{x/y}}$ are the on-site energy of Zn and O, respectively. h_{sp} describes the coupling strength between orbitals located on Zn and O. $h_{sp} = 1$ eV is set artificially and $\varepsilon_{Zn}^{s} - \varepsilon_O^{p} = 4$ eV is obtained by fitting the band gap of mono-ZnO to be 4.0 eV [40]. By diagonalizing the Hamiltonian, the eigenvalues and eigenvectors can be obtained, and then the transition dipole moments and Berry connection can be calculated by the eigenvectors. The obtained valence and conduction bands are shown in Figure 1b.

The equations of motion are modeled by the SBEs, which is written in an instantaneous Bloch basis with laser-system interaction Hamiltonian in length gauge

$$\begin{aligned} i\partial_t \rho_{nm}^{\mathbf{k}(t)} = & \left[\varepsilon_m^{\mathbf{k}(t)} - \varepsilon_n^{\mathbf{k}(t)} - \frac{i(1-\delta_{nm})}{T_2} \right] \rho_{nm}^{\mathbf{k}(t)} \\ & - \mathbf{E}(t) \cdot \sum_{m'} \left[\mathbf{d}_{m'n}^{\mathbf{k}(t)} \rho_{m'm}^{\mathbf{k}} - \mathbf{d}_{mm'}^{\mathbf{k}(t)} \rho_{nm'}^{\mathbf{k}(t)} \right]. \end{aligned} \tag{4}$$

where $m, n \in c, v$ with c representing the conduction band and v representing the valence band. ρ_{cc}, while ρ_{vv} and ρ_{cv} represent the electron density on the conduction band, electron density on the valence band and microscopic polarization between conduction and valence band, respectively. $\mathbf{k}(t) = \mathbf{k_0} + A(t)$ with $A(t)$ being the vector potential. $\vec{E}(t)$ is the

electric field and $\vec{d}_{mn}$ is the complex transition dipole moment between band m and n. The dipole operator is

$$\mathbf{d}_{mn}^{\mathbf{k_0}+\mathbf{A}(t)} = \langle u_m^{\mathbf{k_0}+\mathbf{A}(t)} | \, r \, | u_n^{\mathbf{k_0}+\mathbf{A}(t)} \rangle \approx \quad \langle u_m^{\mathbf{k_0}+\mathbf{A}(t)} | - i\nabla_{\mathbf{k_0}+\mathbf{A}(t)} \, | u_n^{\mathbf{k}+\mathbf{A}(t)} \rangle \, . \tag{5}$$

When $m = n$, $\vec{d}_{mn}$ is the so-called Berry connection. Please note that the intra-band shift operator $i\delta_{mn}\nabla_{\mathbf{k}}\delta(\mathbf{k}-\mathbf{k}')$ has been omitted due to the application of instantaneous basis. The laser-induced current inside the crystal is decomposed into four components according to different mechanisms. The intra-band current reads

$$\mathbf{J}_{\text{intra}}\,(\mathrm{t}) = \sum_{\lambda=c,\mathrm{v}} \int_{BZ} \mathrm{v}_\lambda(\mathrm{k}_0 + \mathrm{A}(\mathrm{t}))\rho_\lambda(\mathrm{k}_0 + \mathrm{A}(\mathrm{t}), \mathrm{t})\mathrm{dk} \tag{6}$$

where $\mathrm{v}_\lambda(\mathrm{k}_0 + \mathrm{A}(\mathrm{t}))$ is the group velocity. The inter-band current reads

$$\mathbf{J}_{\text{inter}}\,(\mathrm{t}) = \frac{\partial}{\partial \mathrm{t}} \int_{BZ} \mathbf{d}_{\mathrm{vc}}(\mathrm{k}_0 + \mathrm{A}(\mathrm{t}))\rho_{\mathrm{cv}}(\mathrm{k}_0 + \mathrm{A}(\mathrm{t}), \mathrm{t})\mathrm{dk} + c.c.. \tag{7}$$

The Berry curvature-induced current reads

$$\mathbf{J}_{\mathrm{Cur}}(\mathrm{t}) = \sum_{\lambda=c,\mathrm{v}} \int_{BZ} \mathbf{E}(t) \times \mathbf{\Omega}_\lambda(\mathrm{k}_0 + \mathrm{A}(\mathrm{t}))\rho_\lambda(\mathrm{k}_0 + \mathrm{A}(\mathrm{t}), \mathrm{t})\mathrm{dk} \tag{8}$$

The current coming from the mixture term reads

$$\mathbf{J}_{\text{mix}}\,(\mathrm{t}) = -\sum_{\mathrm{a}\in\mathrm{x,y}}^{m\neq n} \rho_{\mathrm{nm}}(\mathrm{k}_0 + \mathrm{A}(\mathrm{t}), \mathrm{t})\mathbf{S}_{mn,a}(k_0 + A(t)) \tag{9}$$

where the mixture term is

$$\mathbf{S}_{mn,a}(k) = E^{\mathrm{b}}\left[\frac{\partial d_{\mathrm{mn}}^{\mathrm{b}}}{\partial \mathrm{k_a}} - i d_{\mathrm{mn}}^{\mathrm{b}}(\mathrm{d}_{\mathrm{mm}}^{\mathrm{a}} - d_{\mathrm{nn}}^{\mathrm{a}})\right]\overrightarrow{\mathrm{a}}. \tag{10}$$

The harmonic spectrum can be calculated by the Fourier transform of the current

$$I(\omega) = |\,\mathrm{FT}\{\mathbf{J}(t)\}|^2 \tag{11}$$

where the current can be each of the terms in Equations (3)–(6) or the total current.

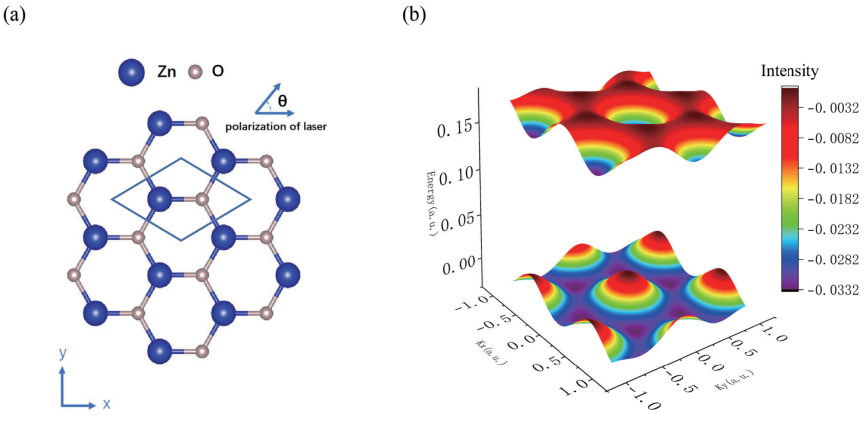

Figure 1. (**a**) Structure of mono-ZnO in real space, the unit vector $a_0 = 3.306$ Å. (**b**) Band structure of mono-ZnO.

3. Results and Discussion

The orientation-dependent high harmonic spectra from different mechanisms are presented in Figure 2 (parallel polarized components) and Figure 3 (perpendicularly polarized components). Firstly, it is certain that Berry curvature term could only generate perpendicularly polarized even harmonics, which originate from odd symmetry of Berry curvature with respect to momentum **k**. For the parallel components, we notice that the orientation-dependent spectra from inter-band, intra-band and mixture current show similar features. From the viewpoint of symmetry properties, there exist mirror symmetry planes which are perpendicular with the laser polarization direction when the driving laser is polarized along 30°, 90° and 150°. The mirror symmetry property leads to the disappearance of even harmonic in the parallel components when the laser polarization is along 30°, 90° and 150°. As a result, the whole orientation feature shows six-fold symmetry, while the odd harmonics are less sensitive to the symmetry property of the sample. It makes sense that even harmonics are always good tools with which to detect symmetry properties of the sample. From another viewpoint, the orientation-dependent feature of elements, such as the transition dipole moments which generate interband HHG components, the derivative of energy band difference between valence and conduction band $\partial\Delta\varepsilon_k/\partial k_{\parallel}(\partial\Delta\varepsilon_k/\partial k_{\perp})$ which would generate intraband HHG components, and the mixture term $\mathbf{S}_{cv,\parallel}(k)$ ($\mathbf{S}_{cv,\perp}(k)$) which would generate the so-called mixture term HHG components, can also help us understand the orientation feature of HHG.The orientation-dependent features of these elements are displayed in Figure 4. It is necessary to emphasize that in Figure 4, the parallel direction is defined as the vector pointing from the Γ to another momentum point, and the perpendicular vector is defined as the anti-clock direction perpendicular to the parallel vector. The absolute values of the paralell parts for both the transition dipole moments, the derivative of energy band $\partial\Delta\varepsilon_k/\partial k_{\parallel}$ and mixture term show six-fold symmetry, which is consistent with the orientation-dependent feature of parallel HHG spectra.

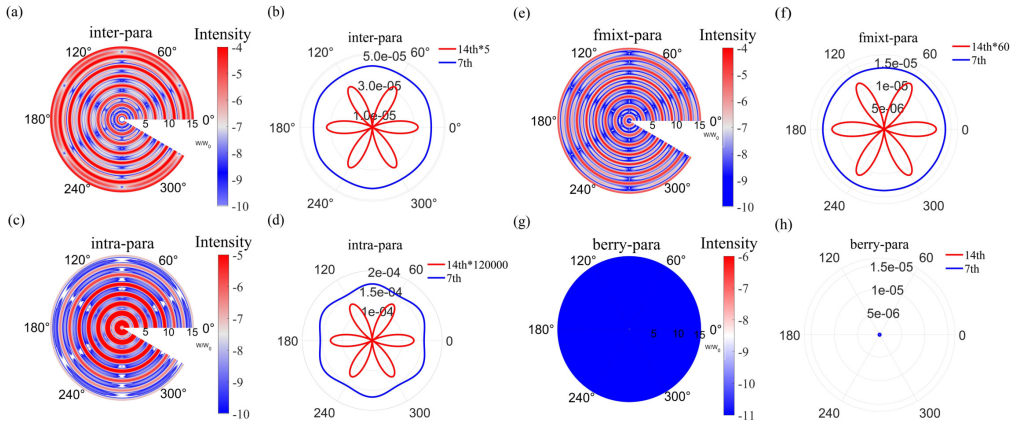

Figure 2. Orientation-dependent parallel polarized HHG specta. (**a**,**b**) are for inter-band components, (**c**,**d**) are for intra-band components, (**e**,**f**) are for mixture term components, (**g**,**h**) Berry curvature components, which are zero.

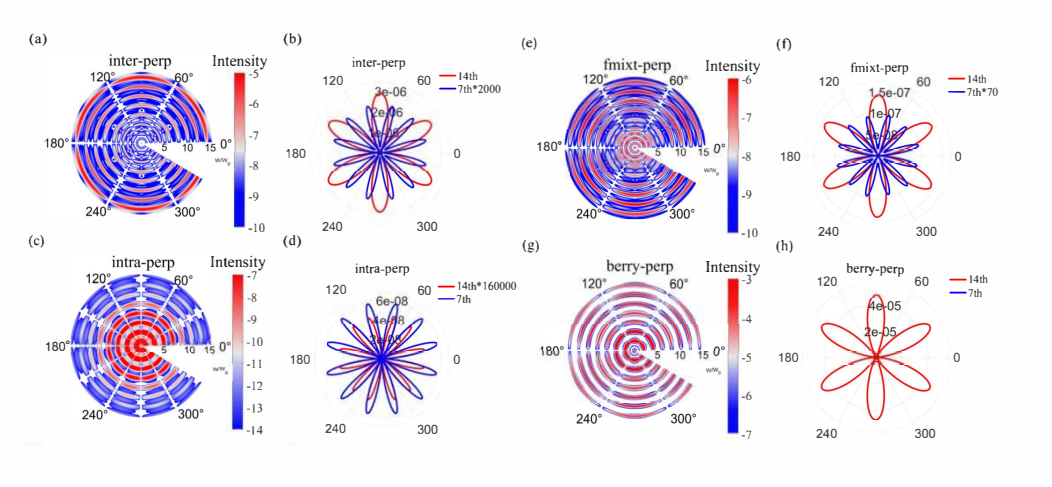

Figure 3. Orientation-dependent perpendicular polarized HHG spectra. (**a**,**b**) are for inter-band components, (**c**,**d**) are for intra-band components, (**e**,**f**) are for mixture term components, (**g**,**h**) Berry curvature components.

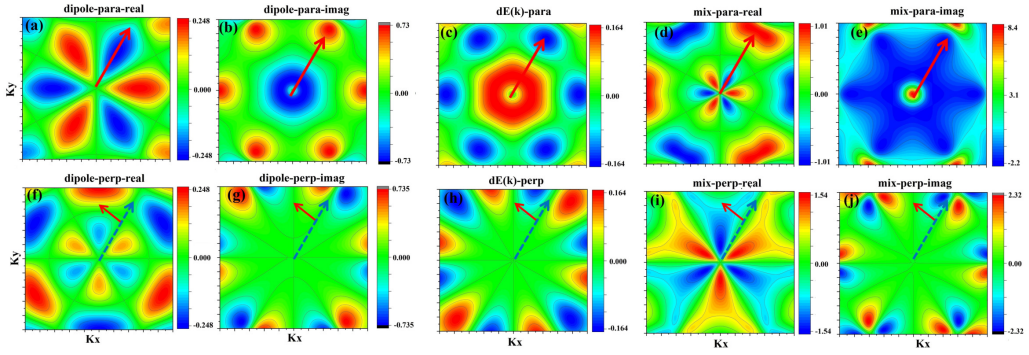

Figure 4. (**a**,**b**) are the real and imaginary parts of parallel transition dipole moments, respectively. (**c**) is the parallel part of derivative of band energy difference. (**d**,**e**) are the real and imaginary parts of parallel mixture term, respectively. (**f**,**g**) are the real and imaginary parts of perpendicular transition dipole moments, respectively. (**h**) is the perpendicular part of derivative of band energy difference. (**i**,**j**) are the real and imaginary parts of perpendicular mixture term, respectively.

The features of perpendicularly polarized components are more complicated. First of all, it is obvious that both the even and odd harmonics are very sensitive to the symmetry properties of the sample. We note that the inter-band and mixture term components in the low-energy regime of Brillouin zone show the same orientation-dependent feature. Even-order harmonics show six-fold symmetry but have 30° mismatching compared with the parallel components, while the odd-order harmonics show twelve-fold symmetry with much weaker intensity. When the laser polarization is along 0°, 60° and 120°, the mirror symmetry plane is parallel with the laser polarization. Maybe it is better to explain the phenomenon using group theory. It is easier to image a classical picture that an electron is driven by the electric field along the direction **a**. Due to its symmetric potential with respect to the electron trajectory, the acceleration perpendicular to the trajectory of the electron should be zero. Thus, there should be only a parallel current, which leads to parallel HHG components only. This is the reason that perpendicular HHG components disappear when the laser polarization is along 0°, 60° and 120°. Due to the inversion mirror symmetry of perpendicular transition dipole moment and mixture term, the odd harmonics of interband mixture components disappear, which leads to twelve-fold symmetry. Since the absolute value of $\partial\Delta\varepsilon_k/\partial k_\perp$ in the whole Brillouin zone shows twelve-fold symmetry, the intra-band

HHG components should have twelve-fold symmetry. Meanwhile, due to the symmetric distribution of $\partial\Delta\varepsilon_k/\partial k_\perp$, the odd-order signals will be dominant.

Figure 5 compares the intensity of the HHG induced by the four different mechanisms. In Figure 5a,c,e, we note that the intensity of parallelly polarized components of the HHG induced by the mixture term (dark blue) is almost the same as the one induced by the inter-band polarization (red) above seventh-order harmonics and also very closely below the seventh-order harmonics, respectively at 0°, 15° and 30°. Additionally, the HHG induced by intra-band currents takes a dominant position above the seventh-order harmonic in the orientation of parallel polarization and becomes smaller than those induced by inter-band polarization and the mixture term below seventh-order harmonics. Similar to the parallelly polarized components, in Figure 5b,d,f, the intensity of perpendicularly polarized components of the HHG induced by the mixture term (dark blue) is nearly identical to the one induced by the inter-band polarization (red) above 10th-order harmonics and also approximate to that below 10th-order harmonics, respectively, at 0°, 15° and 30°. What is different is that, in Figure 5b,d,f, the HHG induced by anomalous currents caused by Berry curvature has the highest intensity in the orientation of perpendicular polarization during the four different mechanisms. Thus, the mixture term HHG cannot be ignored any more in future investigations, especially with regard to the parallel components.

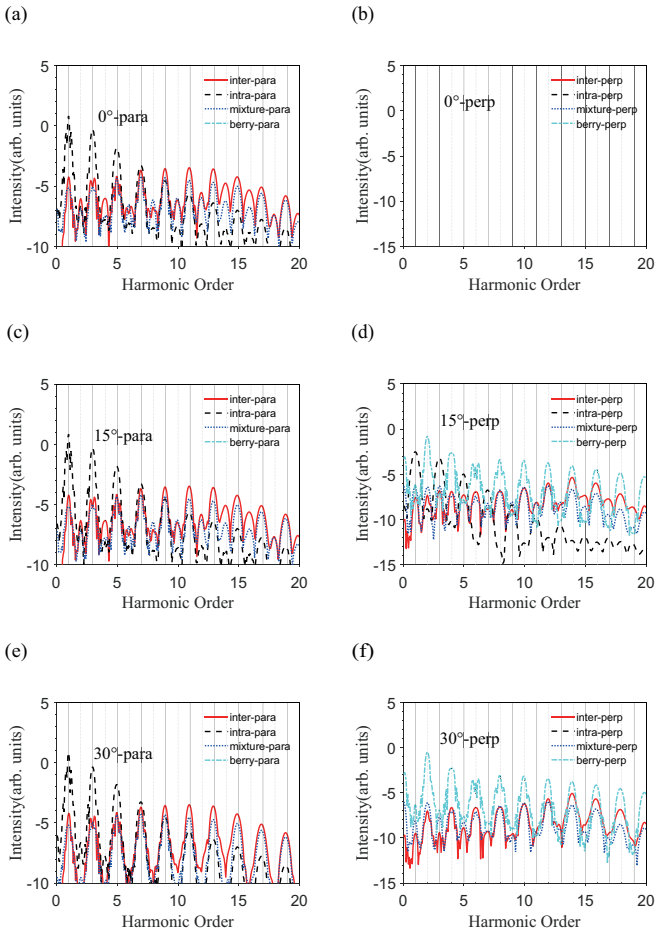

Figure 5. The left side (**a**,**c**,**e**) are the parallel components of HHG spectra from different mechanisms for 0°, 15°, 30°. The right side is the same as the right side (**b**,**d**,**f**), but for perpendicular HHG components.

4. Conclusions

To conclude, this paper investigates the orientation-dependent HHG induced by different mechanisms. There is no doubt that Berry curvature can only generate perpendicular even harmonics and is dominant in the perpendicularly polarized HHG components. In the

parallel components, the intra-band, inter-band and mixture term show same orientation feature. For the perpendicularly polarized HHG components, the interband and mixture term HHG show the same feature, e.g., odd harmonics have twelve-fold symmetry and even harmonics which are stronger than odd harmonics show six-fold symmetry. The intra-band perpendicular components are different from the other mechanisms. Both the even and odd harmonics show twelve-fold symmetry, and odd harmonics are dominant. All these features are analyzed according to the symmetry properties of the sample and the corresponding elements. One more important notice is that in the parallel components, the intensity of the mixture term, which has been ignored for a long time, is close to that of other components. Thus, mixture term will be a non-negligible mechanism in future.

Author Contributions: Simulation and figure preparation, Z.H. and X.X.; writing and editing, S.J., Z.Y. and Y.W.; supervision, Y.W. and S.J.; project administration, Y.W. and S.J. All authors have read and agreed to the published version of the manuscript.

Funding: This research was supported by East China Normal University start-up funding.

Institutional Review Board Statement: Not applicable.

Informed Consent Statement: Not applicable.

Data Availability Statement: Data are available upon request.

Acknowledgments: S.J. Thanks for the fruitful discussion with Lun Yue from Louisiana State University.

Conflicts of Interest: The authors declare no conflict of interest.

References

1. Drescher, M.; Hentschel, M.; Kienberger, R.; Tempea, G.; Spielmann, C.; Reider, G.A.; Corkum, P.B.; Krausz, F. X-ray pulses approaching the attosecond frontier. *Science* **2001**, *291*, 1923–1927. [CrossRef] [PubMed]
2. Paul, P.-M.; Toma, E.S.; Breger, P.; Mullot, G.; Augé, F.; Balcou, P.; Muller, H.G.; Agostini, P. Observation of a train of attosecond pulses from high harmonic generation. *Science* **2001**, *292*, 1689–1692. [CrossRef] [PubMed]
3. Ghimire, S.; DiChiara, A.D.; Sistrunk, E.; Agostini, P.; DiMauro, L.F.; Reis, D.A. Observation of high-order harmonic generation in a bulk crystal. *Nat. Phys.* **2011**, *7*, 138–141. [CrossRef]
4. Schubert, O.; Hohenleutner, M.; Langer, F.; Urbanek, B.; Lange, C.; Huttner, U.; Golde, D.; Meier, T.; Kira, M.; Koch, S.W. Sub-cycle control of terahertz high-harmonic generation by dynamical Bloch oscillations. *Nat. Photonics* **2014**, *8*, 119–123. [CrossRef]
5. Vampa, G.; Hammond, T.; Thiré, N.; Schmidt, B.; Légaré, F.; McDonald, C.; Brabec, T.; Corkum, P. Linking high harmonics from gases and solids. *Nature* **2015**, *522*, 462–464. [CrossRef]
6. You, Y.S.; Reis, D.A.; Ghimire, S. Anisotropic high-harmonic generation in bulk crystals. *Nat. Phys.* **2017**, *13*, 345–349. [CrossRef]
7. Jiang, S.; Gholam-Mirzaei, S.; Crites, E.; Beetar, J.E.; Singh, M.; Lu, R.; Chini, M.; Lin, C. Crystal symmetry and polarization of high-order harmonics in ZnO. *J. Phys. B At. Mol. Opt. Phys.* **2019**, *52*, 225601. [CrossRef]
8. Ndabashimiye, G.; Ghimire, S.; Wu, M.; Browne, D.A.; Schafer, K.J.; Gaarde, M.B.; Reis, D.A. Solid-state harmonics beyond the atomic limit. *Nature* **2016**, *534*, 520–523. [CrossRef]
9. Yoshikawa, N.; Tamaya, T.; Tanaka, K. High-harmonic generation in graphene enhanced by elliptically polarized light excitation. *Science* **2017**, *356*, 736–738. [CrossRef]
10. Liu, H.; Li, Y.; You, Y.S.; Ghimire, S.; Heinz, T.F.; Reis, D.A. High-harmonic generation from an atomically thin semiconductor. *Nat. Phys.* **2017**, *13*, 262–265. [CrossRef]
11. Hafez, H.A.; Kovalev, S.; Deinert, J.-C.; Mics, Z.; Green, B.; Awari, N.; Chen, M.; Germanskiy, S.; Lehnert, U.; Teichert, J. Extremely efficient terahertz high-harmonic generation in graphene by hot Dirac fermions. *Nature* **2018**, *561*, 507–511. [CrossRef] [PubMed]
12. Yoshikawa, N.; Nagai, K.; Uchida, K.; Takaguchi, Y.; Sasaki, S.; Miyata, Y.; Tanaka, K. Interband resonant high-harmonic generation by valley polarized electron–hole pairs. *Nat. Commun.* **2019**, *10*, 3709. [CrossRef] [PubMed]
13. Huang, T.; Zhu, X.; Li, L.; Liu, X.; Lan, P.; Lu, P. High-order-harmonic generation of a doped semiconductor. *Phys. Rev. A* **2017**, *96*, 043425. [CrossRef]
14. Nefedova, V.; Fröhlich, S.; Navarrete, F.; Tancogne-Dejean, N.; Franz, D.; Hamdou, A.; Kaassamani, S.; Gauthier, D.; Nicolas, R.; Jargot, G. Enhanced extreme ultraviolet high-harmonic generation from chromium-doped magnesium oxide. *Appl. Phys. Lett.* **2021**, *118*, 201103. [CrossRef]
15. Bai, Y.; Fei, F.; Wang, S.; Li, N.; Li, X.; Song, F.; Li, R.; Xu, Z.; Liu, P. High-harmonic generation from topological surface states. *Nat. Phys.* **2021**, *17*, 311–315. [CrossRef]
16. Schmid, C.P.; Weigl, L.; Grössing, P.; Junk, V.; Gorini, C.; Schlauderer, S.; Ito, S.; Meierhofer, M.; Hofmann, N.; Afanasiev, D. Tunable non-integer high-harmonic generation in a topological insulator. *Nature* **2021**, *593*, 385–390. [CrossRef]

17. Vampa, G.; Hammond, T.; Thiré, N.; Schmidt, B.; Légaré, F.; McDonald, C.; Brabec, T.; Klug, D.; Corkum, P. All-optical reconstruction of crystal band structure. *Phys. Rev. Lett.* **2015**, *115*, 193603. [CrossRef]
18. Uzan, A.J.; Orenstein, G.; Jiménez-Galán, Á.; McDonald, C.; Silva, R.E.; Bruner, B.D.; Klimkin, N.D.; Blanchet, V.; Arusi-Parpar, T.; Krüger, M. Attosecond spectral singularities in solid-state high-harmonic generation. *Nat. Photonics* **2020**, *14*, 183–187. [CrossRef]
19. Luu, T.T.; Wörner, H.J. Measurement of the Berry curvature of solids using high-harmonic spectroscopy. *Nat. Commun.* **2018**, *9*, 916. [CrossRef]
20. Qiao, Y.; Huo, Y.; Liang, H.; Chen, J.; Liu, W.; Yang, Y.; Jiang, S. Robust retrieval method of crystal transition dipole moments by high-order harmonic spectrum. *Phys. Rev. B* **2023**, *107*, 075201. [CrossRef]
21. Qiao, Y.; Huo, Y.; Jiang, S.; Yang, Y.; Chen, J. All-optical reconstruction of three-band transition dipole moments by the crystal harmonic spectrum from a two-color laser pulse. *Opt. Express* **2022**, *30*, 997. [CrossRef] [PubMed]
22. Qiao, Y.; Chen, J.; Chen, J. Review on the reconstruction of transition dipole moments by solid harmonic spectrum. *Symmetry* **2022**, *14*, 2646. [CrossRef]
23. Corkum, P.B. Plasma perspective on strong field multiphoton ionization. *Phys. Rev. Lett.* **1993**, *71*, 1994. [CrossRef]
24. Krause, J.L.; Schafer, K.J.; Kulander, K.C. High-order harmonic generation from atoms and ions in the high intensity regime. *Phys. Rev. Lett.* **1992**, *68*, 3535. [CrossRef]
25. Ghimire, S.; Ndabashimiye, G.; DiChiara, A.D.; Sistrunk, E.; Stockman, M.I.; Agostini, P.; DiMauro, L.F.; Reis, D.A. Strong-field and attosecond physics in solids. *J. Phys. B At. Mol. Opt. Phys.* **2014**, *47*, 204030. [CrossRef]
26. Vampa, G.; McDonald, C.; Orlando, G.; Klug, D.; Corkum, P.; Brabec, T. Theoretical analysis of high-harmonic generation in solids. *Phys. Rev. Lett.* **2014**, *113*, 073901. [CrossRef] [PubMed]
27. Wu, M.; Ghimire, S.; Reis, D.A.; Schafer, K.J.; Gaarde, M.B. High-harmonic generation from Bloch electrons in solids. *Phys. Rev. A* **2015**, *91*, 043839. [CrossRef]
28. Runge, E.; Gross, E.K. Density-functional theory for time-dependent systems. *Phys. Rev. Lett.* **1984**, *52*, 997. [CrossRef]
29. Tancogne-Dejean, N.; Mücke, O.D.; Kärtner, F.X.; Rubio, A. Impact of the electronic band structure in high-harmonic generation spectra of solids. *Phys. Rev. Lett.* **2017**, *118*, 087403. [CrossRef]
30. Golde, D.; Meier, T.; Koch, S.W. High harmonics generated in semiconductor nanostructures by the coupled dynamics of optical inter-and intraband excitations. *Phys. Rev. B* **2008**, *77*, 075330. [CrossRef]
31. Luu, T.T.; Wörner, H.J. High-order harmonic generation in solids: A unifying approach. *Phys. Rev. B* **2016**, *94*, 115164. [CrossRef]
32. Li, J.; Zhang, X.; Fu, S.; Feng, Y.; Hu, B.; Du, H. Phase invariance of the semiconductor Bloch equations. *Phys. Rev. A* **2019**, *100*, 043404. [CrossRef]
33. Aversa, C.; Sipe, J. Nonlinear optical susceptibilities of semiconductors: Results with a length-gauge analysis. *Phys. Rev. B* **1995**, *52*, 14636. [CrossRef]
34. Wilhelm, J.; Grössing, P.; Seith, A.; Crewse, J.; Nitsch, M.; Weigl, L.; Schmid, C.; Evers, F. Semiconductor Bloch-equations formalism: Derivation and application to high-harmonic generation from Dirac fermions. *Phys. Rev. B* **2021**, *103*, 125419. [CrossRef]
35. Yue, L.; Gaarde, M.B. Introduction to theory of high-harmonic generation in solids: Tutorial. *JOSA B* **2022**, *39*, 535–555. [CrossRef]
36. Yue, L.; Gaarde, M.B. Characterizing Anomalous High-Harmonic Generation in Solids. *Phys. Rev. Lett.* **2023**, *130*, 166903. [CrossRef]
37. Freeman, C.L.; Claeyssens, F.; Allan, N.L.; Harding, J.H. Graphitic nanofilms as precursors to wurtzite films: Theory. *Phys. Rev. Lett.* **2006**, *96*, 066102. [CrossRef]
38. Claeyssens, F.; Freeman, C.L.; Allan, N.L.; Sun, Y.; Ashfold, M.N.; Harding, J.H. Growth of ZnO thin films—Experiment and theory. *J. Mater. Chem.* **2005**, *15*, 139–148. [CrossRef]
39. Tusche, C.; Meyerheim, H.; Kirschner, J. Observation of depolarized ZnO (0001) monolayers: Formation of unreconstructed planar sheets. *Phys. Rev. Lett.* **2007**, *99*, 026102. [CrossRef]
40. Hong, H.-K.; Jo, J.; Hwang, D.; Lee, J.; Kim, N.Y.; Son, S.; Kim, J.H.; Jin, M.-J.; Jun, Y.C.; Erni, R. Atomic scale study on growth and heteroepitaxy of ZnO monolayer on graphene. *Nano Lett.* **2017**, *17*, 120–127. [CrossRef]